https://doi.org/10.5194/egusphere-2026-3702
Preprint. Discussion started: 14 August 2026

Single-Particle Polarization Tomography Enables Highly Accurate Phase Identification of Cloud Particles

Yang Chen[1], Xiang Xu[1*], Ruishan Xiao[1], Fangzhen Yao[1], Xiaojing Shi[1], Jiaxin Wang[1], Jun Wang[1], Gu Liang[2], and Zhiguo Yue[2*]

[1]School of Optoelectronic Science and Intelligent Instrumentation, Xi'an University of Technology, Xi'an 710048, Shaanxi, China.

[2]Weather Modification Center of Shaanxi Province, Xi'an 710016, Shaanxi, China.

Correspondence to: Xiang Xu (xxuxxiang@xaut.edu.cn); Zhiguo Yue (yue_zhiguo@163.com)

Abstract. The phase state of cloud particles and their transformation processes are fundamental to understanding cloud and precipitation formation, variations in radiative energy budgets, and the evolution of severe weather systems. At present, for small-scale cloud particles smaller than 50 μm, conventional identification methods based on morphological features are readily constrained by imaging resolution and feature overlap, making high-accuracy phase discrimination challenging. To address this issue, we propose a polarization tomographic imaging method that integrates digital holography and polarimetric imaging, enabling the simultaneous acquisition of morphological parameters of individual particles within a particle ensemble, including three-dimensional coordinates, particle size, area, perimeter, the major and minor axes of the minimum-area bounding rectangle, and circularity, together with polarization parameters. Through observation experiments in an ice cloud chamber, liquid droplet and ice crystal samples smaller than 50 μm were analyzed. By combining morphological and polarization parameters, accurate identification of liquid droplets and ice crystals in mixed-phase particles was achieved, with an accuracy of 98.33%, representing an improvement of 4.16 percentage points over the conventional circularity-based identification method. In addition, a continuous 10 s observation window during the late stage of mixed-phase cloud glaciation in the ice cloud chamber experiment was selected to calculate liquid water content, the number concentrations of liquid droplets and ice crystals, and their particle-number fractions. The results show that the droplet number concentration and liquid water content decrease with time, whereas the relative fraction of ice crystals gradually increases, reflecting the microphysical process of liquid water conversion into ice in a mixed-phase environment. This method can not only effectively improve the accuracy of phase identification for small-scale cloud particles but also provide information on the microphysical evolution of cloud particles, offering important support for studies of cloud microphysical processes, improvement of model parameterizations, weather modification, and early warning of severe weather events.

1 Introduction

Cloud phase state is a fundamental microphysical parameter that plays a critical role in the initiation, evolution, and dissipation of various weather processes. The spatial distribution of cloud phases and their phase transition processes provide a microscopic perspective for describing cloud and precipitation formation, and are essential for theoretical investigations of

https://doi.org/10.5194/egusphere-2026-3702
Preprint. Discussion started: 14 August 2026

multiple cloud microphysical processes (Morrison et al., 2020; Phillips, 2024). First, accurate detection of mixed-phase clouds is of great importance for assessing the Earth's radiation budget. This is because cloud particles in different phase states exhibit distinct radiative properties, and the phase composition and distribution within clouds significantly influence radiative fluxes at both the top of the atmosphere and the surface (Matus and L'Ecuyer, 2017). Second, precise detection of supercooled liquid water is crucial for understanding precipitation formation. The conversion of small ice crystals into precipitating particles proceeds through three key processes—the Bergeron process, aggregation, and riming growth—each of which depends on supercooled liquid water (Knopf and Alpert, 2023; Zhou et al., 2022a). Furthermore, accurately distinguishing liquid droplets from ice crystals is critical for improving early warning of severe weather events such as snowstorms. Ice multiplication is a major pathway for precipitation enhancement in extreme weather, and its efficiency is governed by the distribution and interactions of supercooled liquid droplets and ice crystals within clouds. Resolving cloud particle phase states therefore allows secondary ice production to be monitored dynamically, leading to improved parameterization of ice multiplication and better forecasts of hazardous weather (Georgakaki et al., 2024; Luke et al., 2021). Finally, precise discrimination between liquid droplets and ice crystals is essential for improving climate models and cloud microphysical parameterizations. Observed ice crystal number concentrations are widely used to evaluate model performance in cloud physics; however, phase misclassification can introduce substantial biases into such evaluations, necessitating reassessment of simulated ice crystal concentrations and refinement of ice-related parameterizations (Wieder et al., 2022; Ewald et al., 2021). High-accuracy phase identification is therefore crucial to improving our understanding of cloud microphysics and cloud–precipitation processes.

At present, methods for cloud-particle phase identification generally fall into two categories: in situ measurements and remote sensing techniques. In situ approaches mainly rely on instruments such as the Cloud Imaging Probe (CIP), the Precipitation Imaging Probe (PIP) (Pettersen et al., 2021), and two-dimensional cloud and precipitation probes (2D-C and 2D-P) to obtain direct images of cloud particles (Gaudek et al., 2026), from which phase is inferred on the basis of particle morphology (Pettersen et al., 2021; D'Alessandro et al., 2023). However, the limited resolution of optical imaging systems prevents reliable characterization of particle morphology for particles smaller than 50 μm, thereby increasing the risk of phase misclassification and reducing identification accuracy. By contrast, remote sensing techniques offer the advantages of non-contact operation and broad spatial coverage. These techniques distinguish particle phase through differences in backscattered signals associated with the contrasting morphologies of liquid droplets and ice crystals (Qi et al., 2021; Xiao et al., 2023). For example, polarization lidar uses the ratio of cross-polarized to co-polarized backscattered signals—the depolarization ratio—to identify particle phase (Shishko et al., 2023; Ma et al., 2025). However, this method has notable limitations. Inversion of the lidar equation relies on a priori assumptions about the relationship between extinction and backscattering, potentially introducing uncertainty into the retrievals (Xu et al., 2025; Huang et al., 2023). Moreover, because polarization lidar measures the bulk polarization properties of particle ensembles, it cannot readily resolve polarization at the single-particle level (Dubovik et al., 2019). For particles smaller than 50 μm, multiple scattering further complicates the accurate retrieval of polarization parameters such as the depolarization ratio (Shcherbakov et al., 2024). Accurate phase identification of cloud particles in this size range therefore remains a major challenge in atmospheric remote sensing and cloud physics.

https://doi.org/10.5194/egusphere-2026-3702
Preprint. Discussion started: 14 August 2026

Digital holography is a rapid, real-time, non-contact, full-field optical method widely used to probe dynamic processes in cells, flow fields, and moving particles (Zhang et al., 2012; Liu et al., 2021). It permits precise three-dimensional localization of individual particles within the field of view while simultaneously resolving their microphysical properties (Pan et al., 2021). Beyond intensity information alone, polarimetric imaging provides multidimensional information about the internal microstructure and external texture of a target (Yan et al., 2023). Integrating polarization with holographic imaging therefore enables simultaneous retrieval of morphological and polarization properties at the single-particle level. This polarization tomographic imaging method allows these complementary features to be characterized jointly, offering a new avenue for cloud-particle phase identification. In recent years, polarization holography has attracted increasing attention in both development and application. However, in nearly all existing studies, polarization has been used primarily as an auxiliary component of holographic imaging. For example, polarization multiplexing exploits different polarization states as independent information channels to record multiple holograms simultaneously within the same medium, thereby increasing storage density (Hong et al., 2017; Wang et al., 2024). Polarization phase-shifting has also been used to suppress zero-order diffraction and improve image quality (Liu et al., 2023), whereas polarization-dependent differences among samples have been exploited to enhance holographic contrast (Behal et al., 2022; Cazac et al., 2025). Nevertheless, rapid retrieval of the Stokes vector of the target remains a major challenge, and studies addressing this problem remain scarce.

Here we present a particle observation method based on polarization tomographic imaging that integrates digital holography with polarimetric imaging. This approach enables precise localization of individual particles within an ensemble while simultaneously retrieving their three-dimensional coordinates and a broad suite of microphysical properties, including nine morphological parameters—such as projected-area equivalent diameter, the major and minor axes of the minimum-area bounding rectangle, perimeter, area, and circularity—as well as four polarization parameters, namely the Stokes vector components (S_0, S_1, and S_2) and the degree of linear polarization (DoLP). Using the developed system, we conducted cloud-chamber experiments on both liquid droplets and ice crystals, enabling simultaneous characterization of their morphological and polarization properties.

The experimental results show that the mean particle size was 4.66 μm for liquid droplets and 25.36 μm for ice crystals, with both populations predominantly smaller than 50 μm. Further analysis revealed distinct differences in circularity and DoLP between the two particle types. However, because the distributions of each parameter still overlapped between liquid droplets and ice crystals, complete phase identification could not be achieved using either parameter alone. We therefore combined circularity and DoLP for phase identification, which substantially improved performance. A linear support vector machine (SVM) was then applied to the two-parameter space to derive the corresponding decision function. Compared with single-parameter methods, this dual-parameter SVM method achieved a classification accuracy of 98.33%. The incorporation of polarization information thus improves phase identification beyond conventional morphology-based methods, enabling reliable identification of liquid droplets and ice crystals smaller than 50 μm. These results provide high-precision data for studies of cloud microphysical processes and model evaluation, and offer a promising new observational approach for applications including severe weather forecasting and weather modification.

https://doi.org/10.5194/egusphere-2026-3702
Preprint. Discussion started: 14 August 2026

2 Methods and principles

2.1 Polarization effects of birefringent crystals

When a linearly polarized beam propagates through a birefringent crystal, its polarization state changes because of the crystal's intrinsic anisotropy. The incident light is decomposed into two orthogonally polarized components, namely the ordinary (o) and extraordinary (e) rays, which propagate through the crystal with different phase velocities, thereby giving rise to a phase retardation (Lane et al., 2021; Born and Wolf, 2013). Liquid droplets are optically isotropic, with randomly arranged water molecules and a refractive index that remains constant during propagation; consequently, they do not exhibit birefringence and leave the incident polarization state unchanged. Ice crystals, however, are anisotropic birefringent media with well-defined lattice structures. Their refractive indices vary with both the propagation direction and the polarization direction of the incident light, giving rise to phase retardation. The resulting phase retardation, denoted by δ, is given by Eq. (1):

$$\delta = \frac{2\pi}{\lambda}\Delta n d \tag{1}$$

where λ is the wavelength of the incident light; n_o and n_e are the refractive indices of the ordinary and extraordinary rays, respectively; $\Delta n = n_e - n_o$ denotes the birefringence, that is, the difference between n_e and n_o; and d is the crystal thickness.

Let β denote the angle between the crystal optical axis and the reference coordinate system, typically defined by the detector plane. The Mueller matrix of the birefringent crystal can then be written as (Fuller, 1995; Bass et al., 1995):

$$\boldsymbol{M}(\delta) = \begin{bmatrix} 1 & 0 & 0 & 0 \\ 0 & cos^2 2\beta + sin^2 2\beta cos\delta & sin2\beta cos2\beta(1 - cos\delta) & -sin2\beta sin\delta \\ 0 & sin2\beta cos2\beta(1 - cos\delta) & sin^2 2\beta + cos^2 2\beta cos\delta & cos2\beta sin\delta \\ 0 & sin2\beta sin\delta & -cos2\beta sin\delta & cos\delta \end{bmatrix} \tag{2}$$

where δ is the phase retardation and β is the angle between the crystal optical axis and the reference coordinate system.

Assuming that the incident light is fully linearly polarized, with its polarization direction making an angle α with respect to the reference coordinate system, the Stokes vector Sin of the incident light can be written as:

$$\boldsymbol{S}_{in} = I_0 \begin{bmatrix} 1 \\ cos2\alpha \\ sin2\alpha \\ 0 \end{bmatrix} \tag{3}$$

where I_0 denotes the intensity of the incident light. After passing through the birefringent crystal, the Stokes vector $\boldsymbol{S}_{out}$ of the transmitted light can be written as:

$$\boldsymbol{S}_{out} = \boldsymbol{M}(\delta)\boldsymbol{S}_{in} \tag{4}$$

The individual components S_0, S_1, and S_2 of $\boldsymbol{S}_{out}$ are given by:

https://doi.org/10.5194/egusphere-2026-3702
Preprint. Discussion started: 14 August 2026

$$S_0^{out} = I_0 \tag{5}$$

$$S_1^{out} = I_0[cos2\alpha(cos^2 2\beta + sin^2 2\beta cos\delta) + sin2\alpha sin2\beta cos2\beta(1 - cos\delta)] \tag{6}$$

$$S_2^{out} = I_0[cos2\alpha sin2\beta cos2\beta(1 - cos\delta) + sin2\alpha(sin^2 2\beta + cos^2 2\beta cos\delta)] \tag{7}$$

The degree of linear polarization (DoLP) of the transmitted light is defined as (where S_0, S_1, and S_2 denote the components of $\boldsymbol{S}_{out}$):

$$DoLP_{biref} = \frac{\sqrt{(S_1^{out})^2 + (S_2^{out})^2}}{S_0^{out}} \tag{8}$$

Substituting Eqs. (5–7) into Eq. (8) and simplifying yields:

$$DoLP_{biref} = \sqrt{1 - sin^2(2\alpha - 2\beta)sin^2\left(\frac{\delta}{2}\right)} \tag{9}$$

When the Stokes vector is measured using a photoelectric detection system, its four parameters can also be expressed in terms of intensity differences (Zhou et al., 2022b):

$$\boldsymbol{S} = \begin{bmatrix} S_0 \\ S_1 \\ S_2 \\ S_3 \end{bmatrix} = \begin{bmatrix} I_{0^\circ} + I_{90^\circ} \\ I_{0^\circ} - I_{90^\circ} \\ I_{45^\circ} - I_{135^\circ} \\ I_R - I_L \end{bmatrix} \tag{10}$$

where $I_{0°}$, $I_{45°}$, $I_{90°}$, and $I_{135°}$ are intensities measured through linear analyzers oriented at 0°, 45°, 90°, and 135°, respectively; I_R and I_L denote right- and left-circularly polarized intensity components. Since DoLP only requires S_0, S_1, and S_2, only these three components are used in subsequent analysis.

The degree of linear polarization (DoLP) is then given by:

$$DoLP = \frac{\sqrt{S_1^2 + S_2^2}}{S_0} \tag{11}$$

The birefringent crystal modifies the polarization state of the incident light by introducing a phase retardation δ. Its polarization effect is fully described by the Mueller matrix in Eq. (2), and the degree of linear polarization of the transmitted light is given by Eq. (9).

By contrast, liquid droplets have a single refractive index and do not exhibit birefringence; consequently, they do not alter the polarization state of the incident light. Scattering by a liquid droplet changes only the propagation direction and polarization orientation of the light, without degrading its polarization state. In other words, the scattered light remains fully polarized (Donovan et al., 2015). Unlike ice crystals, liquid droplets do not introduce birefringence-induced phase retardation (that is, δ = 0) and therefore do not generate additional depolarization.

https://doi.org/10.5194/egusphere-2026-3702
Preprint. Discussion started: 14 August 2026

For fully linearly polarized incident light, the Stokes vector of the light scattered by a liquid droplet can be written as:

$$\boldsymbol{S}_{out} \frac{1}{k^2 r^2} \boldsymbol{M}(\theta) \boldsymbol{S}_{in} \tag{12}$$

where $M(\theta)$ is the Mueller matrix, that contains the information on how the particle modulates the polarization state, Sin is the Stokes vector of the incident light defined in Eq. (3), and θ is the scattering angle. $k = 2\pi / \lambda$ is the wavenumber, and r is the observation distance. The factor $1 / (k^2 r^2)$ accounts for the attenuation of light intensity with distance.

According to Mie scattering theory, the Mueller scattering matrix for spherical liquid droplets can be expressed as:

$$\boldsymbol{M}(\theta) = \begin{bmatrix} M_{11}(\theta) & M_{12}(\theta) & 0 & 0 \\ M_{12}(\theta) & M_{11}(\theta) & 0 & 0 \\ 0 & 0 & M_{33}(\theta) & M_{34}(\theta) \\ 0 & 0 & -M_{34}(\theta) & M_{33}(\theta) \end{bmatrix} \tag{13}$$

where $M_{ij}(\theta)$ (i, j = 1, 2, 3, 4) are angle-dependent elements of the Mueller scattering matrix determined by Mie theory.

For spherical droplets, the scattering properties are fully described by Mie theory. Under linearly polarized illumination, the Stokes vector is given by Eq. (3). Combining Eqs. (3) and (13) yields the components of $\boldsymbol{S}_{out}$ as follows:

$$\begin{aligned} S_0^{out} &= M_{11} + M_{12} cos2\alpha \\ S_1^{out} &= M_{12} + M_{11} cos2\alpha \\ S_2^{out} &= M_{33} sin2\alpha \end{aligned} \tag{14}$$

The degree of linear polarization (DoLP) of the scattered light can then be expressed as:

$$DoLP_{lin}(\theta, \alpha) = \frac{\sqrt{(M_{12} + M_{11} cos2\alpha)^2 + (M_{33} sin2\alpha)^2}}{M_{11} + M_{12} cos2\alpha} \tag{15}$$

where α denotes the angle between the incident polarization direction and the reference coordinate axis.

2.2 Principles of digital holography

Under plane-wave illumination, light diffracted by the particles is treated as the object wave, whereas light that does not interact with the particles and is directly received by the detector serves as the reference wave. Their interference is recorded as a hologram, which is then numerically reconstructed using the Fresnel–Kirchhoff diffraction integral (Pan et al., 2021). For a hologram containing multiple particles, the intensity distribution $U_R(u, v)$ on the reconstruction plane is given by

$$U_R(u, v) = \frac{1}{j\lambda} \iint_{\infty} R(x, y) I_H(x, y) \frac{exp\left(jk\sqrt{(u-x)^2 + (v-y)^2 + Z_r^2}\right)}{\sqrt{(u-x)^2 + (v-y)^2 + Z_r^2}} dxdy \tag{16}$$

where λ is the wavelength, j is the imaginary unit, R(x, y) is the reference wave, and $I_H(x, y)$ is the intensity of the interference fringes recorded on the sensing medium. Here, k denotes the wavenumber; x and y are the horizontal and vertical coordinates in the particle focal plane, respectively; whereas u and v are the corresponding coordinates in the hologram

https://doi.org/10.5194/egusphere-2026-3702
Preprint. Discussion started: 14 August 2026

reconstruction plane. Z_r denotes the reconstruction distance, taking discrete values Z_i (i = 1, 2, 3, …) corresponding to different reconstruction planes (Gao et al., 2022). Particles located on a given reconstruction plane appear sharply focused, whereas those away from that plane are blurred. By reconstructing each hologram numerically at different distances Z_i, the three-dimensional positions of particles at different times can be recovered (Singh and Panigrahi, 2010).

In image analysis, polygonal approximation is commonly used to simplify particle contours by reducing the number of contour vertices. For small particles, shape is characterized using the minimum-area bounding rectangle, determined with the rotating calipers algorithm by rotating a bounding rectangle around the contour and selecting the one with the smallest area (Aviles and Lear, 2025; Yan et al., 2022). Compared with other methods, this approach offers advantages in both computational efficiency and accuracy. After particle localization, a set of geometric parameters can be extracted, including the centroid coordinates (x, y, z), area S_i, perimeter L_i, major-axis length L, minor-axis length W and projected-area equivalent diameter D_{eq}. The projected-area equivalent diameter was calculated from the segmented particle area as

$$D_{eq} = \frac{2}{M}\sqrt{\frac{A_p p^2}{\pi}} \tag{17}$$

where A_p is the projected particle area in pixels, p = 3.45 μm is the camera pixel size, and M = 5 is the imaging magnification.

Circularity F is then calculated from the corresponding expression; for an ideal spherical particle, F = 4, with larger values indicating greater departure from circularity (Huang and Lei, 2020).

$$F = \frac{L \times L_i}{S_i} \tag{18}$$

After obtaining the morphological parameters of individual particles, the microphysical statistical parameters of the particle ensemble can be further calculated by combining the particle phase-identification results. This study mainly focuses on the number concentrations of liquid droplets and ice crystals, as well as liquid water content (LWC). Number concentration represents the number of particles per unit sampling volume and is an important parameter for describing the distribution characteristics of cloud particle ensembles. For continuous observations over a given time period, the particle number concentration can be expressed as

$$N_c = \frac{1}{V}\sum_{i=1}^{k} n_i \tag{19}$$

Where N_c is the particle number concentration, V is the cumulative sampling volume corresponding to the given time period, n_i is the number of particles identified in frame i, and k is the number of image frames included in the statistics.

Liquid water content represents the mass of liquid water per unit volume of air and is an important cloud microphysical parameter for characterizing the amount and evolution of supercooled liquid water. Based on the equivalent diameters of particles identified as liquid droplets, and assuming that the droplets are approximately spherical, LWC can be calculated as

https://doi.org/10.5194/egusphere-2026-3702
Preprint. Discussion started: 14 August 2026

$$\mathrm{LWC} = \sum_{i=1}^{N} \frac{4\pi\rho_c}{3V}\left(\frac{d_i}{2}\right)^3 \tag{20}$$

where ρ_c is the density of water, V is the sampling volume, d_i is the projected-area equivalent diameter of droplet i, and N is the total number of droplets included in the statistics. If time-binned statistics are performed for consecutive image frames, V is taken as the cumulative sampling volume corresponding to all images within that time period.

3 Experimental System

In this study, we propose for the first time a polarization tomographic imaging method based on the principles of digital holography and polarimetric imaging. This method enables the simultaneous retrieval of morphological and polarization parameters of individual particles. The experimental setup is shown in Fig. 1.

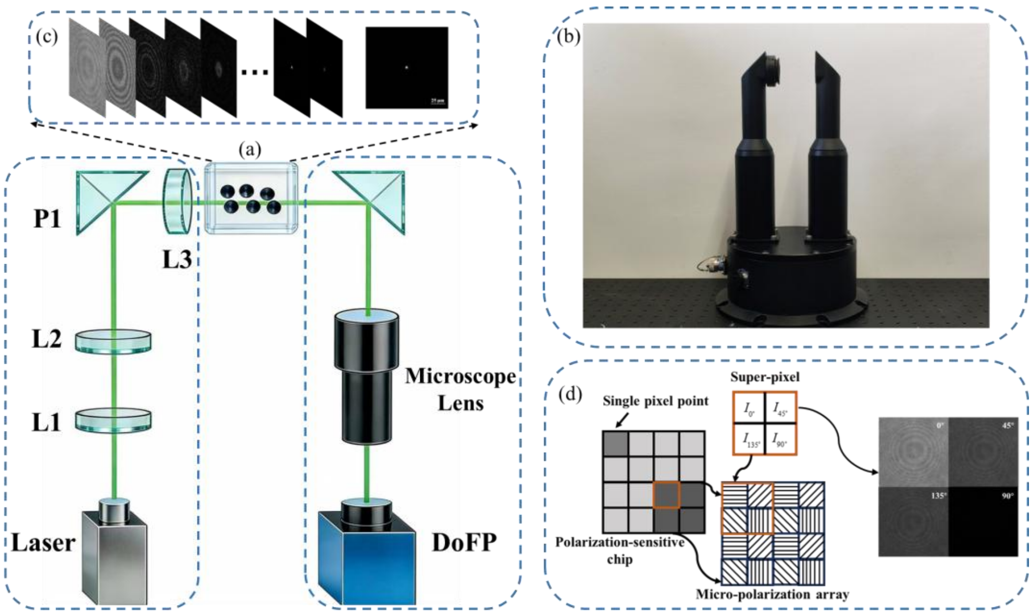

Figure 1: Polarization tomographic imaging system. (a) Schematic diagram of the system; (b) photograph of the polarization tomographic imager; (c) numerical reconstruction process of particles; (d) working principle of the division-of-focal-plane polarization camera.

The working principle of polarization tomographic imaging is illustrated in Fig. 1a. A pulsed laser with a central wavelength of 520 nm, a pulse width of 300 ns, and a pulse repetition interval of 80 µs was used as the light source, making it suitable for observing transient particles and dynamic processes. The emitted beam was expanded by lens L1 and collimated by lens L2 to form a parallel beam. After redirection by a right-angle prism P1, the beam passed through a linear polarizer (L3) with an extinction ratio greater than 1000:1, producing highly pure linearly polarized light. This linearly polarized beam then illuminated the particle measurement region. Light diffracted by the particles served as the object wave, whereas transmitted light that did not interact with the particles served as the reference wave. The interference between these two components was

https://doi.org/10.5194/egusphere-2026-3702
Preprint. Discussion started: 14 August 2026

formed at the focal plane of the imaging lens and recorded as a polarization tomographic image. A 5× telecentric lens (WWK50-102-111V3), with a working distance of 102 mm and support for a maximum sensor size of 1.1 inches, was used in the imaging system. The lens provides megapixel-level resolution, low distortion (0.16%), and high telecentricity (0.18%). The interference patterns were recorded by a division-of-focal-plane (DoFP) polarization camera, in which a micropolarizer array is integrated directly onto the imaging plane. This configuration enables simultaneous acquisition of intensity information at four polarization orientations (0°, 45°, 90°, and 135°), as shown in Fig. 1d. Figure 1b shows the fabricated polarization tomographic imager developed on the basis of the principle illustrated in Fig. 1a.

Using the polarization tomography imaging system described above, observation experiments of droplets and ice crystals were conducted in an ice cloud chamber. The experimental environment and working procedure of the ice cloud chamber are shown in Fig. A1. Under low-temperature conditions (−25 °C), after fog had been generated by the atomizer but before catalyst injection, only supercooled liquid droplets were present in the chamber. After catalyst introduction, the supercooled droplets underwent heterogeneous nucleation on the catalyst particles, leading to ice crystal formation and the development of a mixed-phase state in which liquid droplets and ice crystals coexisted.

4 Results

The polarization tomographic images of liquid droplets and ice crystals acquired in the cloud chamber were processed to simultaneously retrieve the morphological and polarization parameters of individual particles within the field of view.

First, the particle-containing holograms were numerically reconstructed to convert the recorded two-dimensional holographic information into a three-dimensional representation, thereby yielding accurate particle positions and the corresponding intensity distributions. Reconstruction was performed using the angular spectrum method. Along the optical axis (z-axis), 35 intensity images were reconstructed at 1 mm intervals over a range of 0–34 mm. Figure 1c shows an example of how the intensity distribution of a single liquid droplet varies across different reconstruction planes.

Subsequently, the exact reconstruction plane of each particle was identified from the 35 intensity images to obtain the in-focus image for subsequent extraction of morphological and polarization parameters. This was achieved using a local intensity gradient variance method. Specifically, a local pixel region corresponding to the particle in the x and y directions was selected, and the local intensity gradient variance within this region was calculated for each reconstructed image. The plane with the maximum variance was taken as the focal plane. On this basis, the three-dimensional coordinates of the particle were determined, including its focal plane and precise position within that plane. As shown in Fig. 1c, the rightmost image corresponds to the true focal plane of the particle and thus represents its accurate intensity distribution.

After identifying the focal plane of each particle, the corresponding morphological and polarization parameters were extracted. Figure 2 summarizes the extraction of morphological parameters for four representative particles, including one liquid droplet (a) and three ice crystals (b–d). The in-focus intensity images were first binarized, followed by edge smoothing using morphological opening and closing operations to obtain closed particle contours. For particles with internal cavities, a

https://doi.org/10.5194/egusphere-2026-3702
Preprint. Discussion started: 14 August 2026

hole-filling algorithm was applied to ensure complete morphological representation. The final particle identification results are shown in Figs. 2(a–4), 2(b–4), 2(c–4), and 2(d–4).

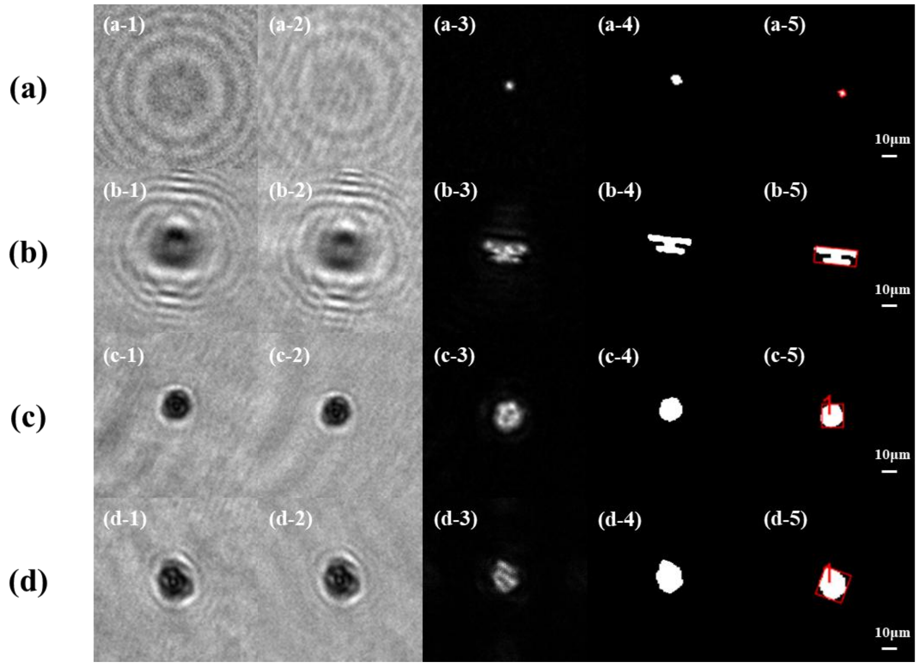

Figure 2: Morphological analysis results of individual particles. (a–1), (b–1), (c–1), and (d–1) raw tomographic images of particles; (a–2), (b–2), (c–2), and (d–2) background-corrected particle images; (a–3), (b–3), (c–3), and (d–3) in-focus particle images; (a–4), (b–4), (c–4), and (d–4) particle segmentation results; (a–5), (b–5), (c–5), and (d–5) minimum bounding rectangles of particles.

After particle identification, particle labeling and external contour extraction were performed to derive the morphological parameters of each target particle. The projected area was first calculated from the number of pixels occupied by the particle. The projected-area equivalent diameter was then calculated from the segmented projected area. The minimum-area bounding rectangle was determined, from which the major and minor axes were obtained. In total, nine morphological parameters were extracted, including the three-dimensional coordinates, projected-area equivalent diameter, projected area, perimeter, and the major and minor axes of the bounding rectangle. The circularity F was subsequently calculated using Eq. (18), completing the morphological parameter extraction for each particle. The morphological parameters of the four particles shown in Fig. 2 are provided in Table B1.

To validate the accuracy of the measurement system and the multidimensional parameter extraction algorithm, and to further support its application in cloud chamber particle characterization, calibration experiments were conducted using standard glass microspheres (nominal diameters of 5.1 ± 0.5 μm, 10.0 ± 1.0 μm, and 49.0 ± 1.4 μm) and ultrasonically generated droplets (nominal median diameter of 3.9 μm, uncertainty ±25%). The results are shown in Fig. 3a–d. The measured diameters of the standard microspheres all fell within their certified uncertainty ranges. For the atomized droplets, the measured median diameter agreed well with the nominal value, and more than 70% of the droplets were smaller than 5 μm, confirming the reliability of the system. We then extracted morphological parameters for 400 particles generated in the ice cloud chamber,

https://doi.org/10.5194/egusphere-2026-3702
Preprint. Discussion started: 14 August 2026

including 200 liquid droplets and 200 ice crystals; the resulting equivalent-diameter distributions are shown in Fig. 3e and 3f. Droplet sizes ranged from 2.7–8.9 μm, with a mean of 4.66 μm (SD = 1.05 μm) and a coefficient of variation of 22.6%, consistent with the preset chamber conditions. After heterogeneous nucleation, newly formed ice crystals grew progressively through deposition, aggregation, and riming, resulting in a broader size distribution. Ice crystal sizes ranged from 8.9–53.3 μm, with a mean of 25.36 μm (SD = 8.72 μm) and a coefficient of variation of 34.4%. In the present experiments, the measured particle sizes were predominantly smaller than 50 μm. This size range remains a major challenge for current cloud particle phase identification. The proposed method nevertheless enables effective measurement and parameter extraction in this regime, underscoring its strong potential for cloud particle phase discrimination.

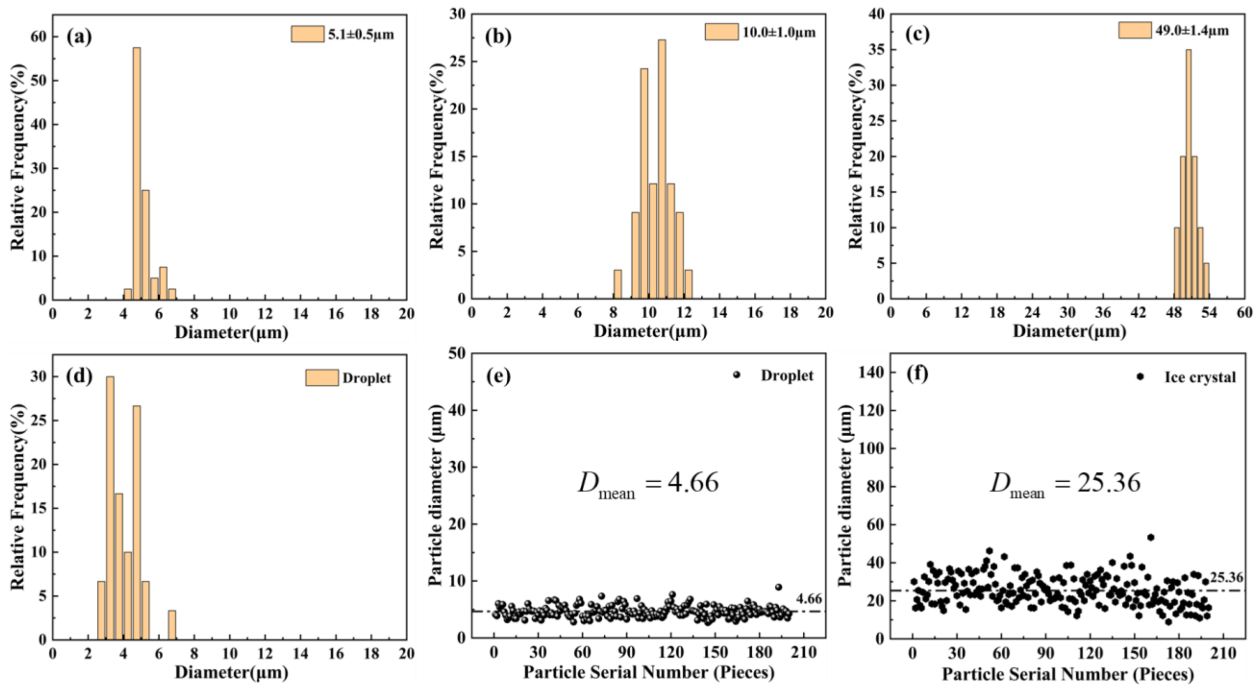

Figure 3: Particle-size measurement results. (a) Standard particles with a diameter of 5.1 ± 0.5 μm; (b) standard particles with a diameter of 10.0 ± 1.0 μm; (c) standard particles with a diameter of 49.0 ± 1.4 μm; (d) ultrasonically generated droplets; (e) size distribution scatter plot of liquid droplets in the cloud chamber; (f) size distribution scatter plot of ice crystals in the cloud chamber.

Liquid droplets are typically near-spherical because of surface tension and therefore exhibit regular shapes with smooth boundaries. Ice crystals, by contrast, form through more complex growth pathways and often display irregular morphologies, including columnar, plate-like, and needle-like structures. Circularity quantifies deviation from an ideal circular projection and is therefore well suited to distinguishing liquid droplets from ice crystals. As shown in Fig. 4, circularity differs significantly between liquid droplets and ice crystals. The circularity values of liquid droplets are mainly distributed between 2.5 and 4.5, with a mean of 3.32 (SD = 0.42) and a coefficient of variation of 12.6%, indicating relatively regular shapes and high sphericity. In contrast, ice crystals show higher circularity values, mainly distributed between 4.0 and 9.0, with a mean of 6.30 (SD =

https://doi.org/10.5194/egusphere-2026-3702
Preprint. Discussion started: 14 August 2026

1.79) and a coefficient of variation of 28.4%. The substantially larger values and broader distribution observed for ice crystals reflect their greater morphological complexity and diversity.

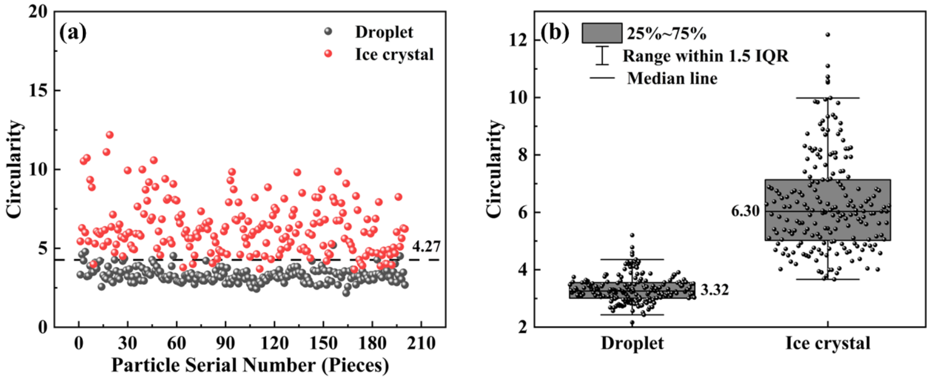

Figure 4: (a) Scatter plot of circularity for liquid droplets and ice crystals; (b) box plot of circularity distributions for liquid droplets and ice crystals.

Further statistical analysis indicates that a circularity threshold of 4.27 can separate most liquid droplets from ice crystals. However, an overlap region between the two distributions remains. Ice crystals within this region were analyzed further, as shown in Fig. 5. Because these particles exhibit morphologies similar to those of liquid droplets, they are susceptible to misclassification when phase identification is based on shape alone. This result highlights a key limitation of image-based cloud particle phase identification: when liquid droplets and ice crystals share similar morphologies, or when particle sizes approach the resolution limit of the imaging system, a single morphological parameter is insufficient for reliable phase identification.

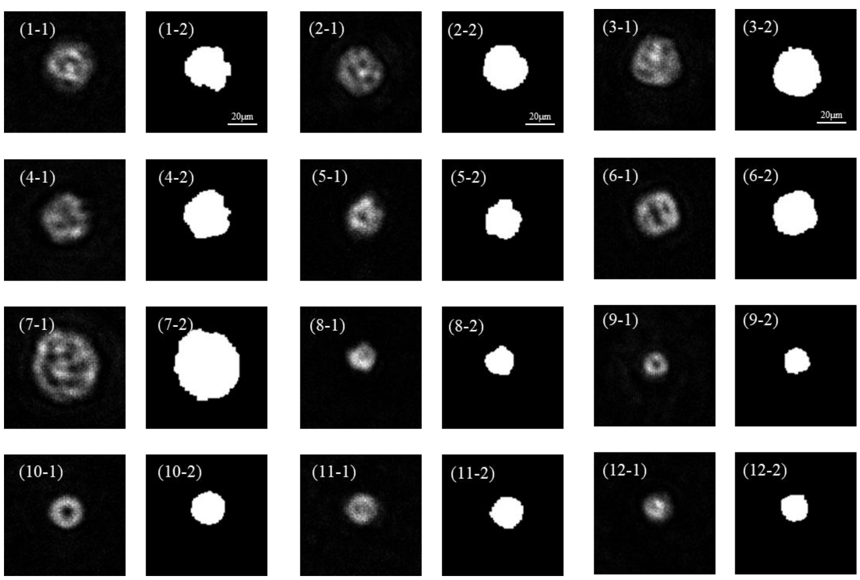

Figure 5: In-focus images and corresponding segmentation results of ice crystals with circularity similar to those of liquid droplets.

https://doi.org/10.5194/egusphere-2026-3702
Preprint. Discussion started: 14 August 2026

To overcome the limitations of morphology-based identification, we further calculated particle polarization information, particularly the degree of linear polarization (DoLP), as a complementary feature for phase discrimination. Using the in-focus images obtained after focus determination—that is, the accurately reconstructed intensity distributions—the Stokes parameters (S_0, S_1, and S_2) of liquid droplets and ice crystals were calculated according to Eq. (10), and the DoLP was subsequently derived using Eq. (11). The resulting polarization information is shown as pseudo-color images in Fig. 6, where color intensity within each particle indicates the magnitude of the polarization parameters, with darker colors corresponding to higher values.

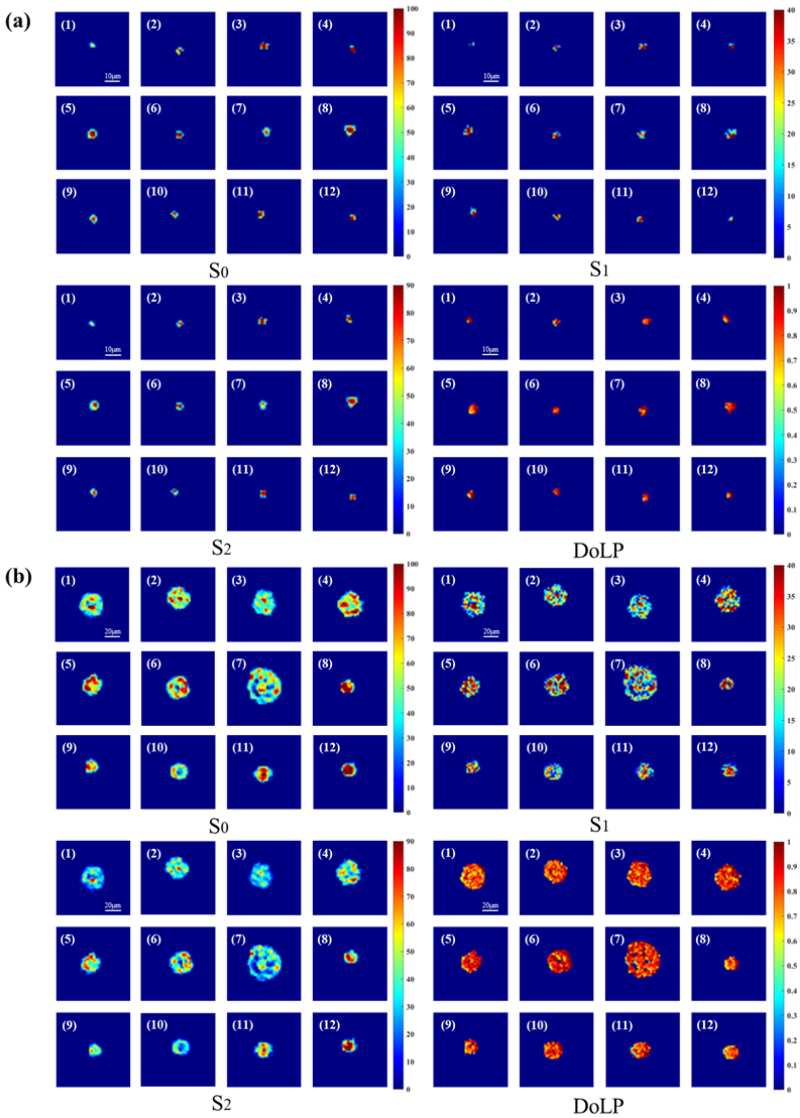

Figure 6: (a) Pseudo-color image of polarization parameters for a liquid droplet; (b) pseudo-color image of polarization parameters for an ice crystal.

https://doi.org/10.5194/egusphere-2026-3702
Preprint. Discussion started: 14 August 2026

To overcome the limitations of the circularity when particle morphologies are similar, we further analyzed the degree of linear polarization (DoLP) for 400 particles. Because DoLP is sensitive to both particle shape and internal structure, it provides complementary information that can reduce misclassification and improve phase discrimination. The distributions are shown in Fig. 7. Liquid droplets generally exhibited higher DoLP values than ice crystals: the DoLP values of the 200 liquid droplets were mainly distributed between 0.78 and 0.96, with an arithmetic mean of 0.857, whereas the 200 ice crystals were mainly distributed between 0.66 and 0.82, with an arithmetic mean of 0.742. As shown in Fig. 7b, the two particle types show distinct DoLP distributions, although partial overlap remains. This contrast arises from their different optical properties. As optically isotropic media, liquid droplets primarily change the propagation direction of scattered light while largely preserving the incident linear polarization state. Ice crystals, by contrast, are birefringent: incident linearly polarized light is decomposed into ordinary and extraordinary components that propagate with different phase velocities, generating phase retardation and partially converting linear polarization into elliptical polarization (Schlimme et al., 2005; Jordan et al., 2019). As a result, the DoLP of light scattered by ice crystals is generally lower. These results demonstrate that DoLP is a powerful polarization parameter for distinguishing liquid droplets from ice crystals.

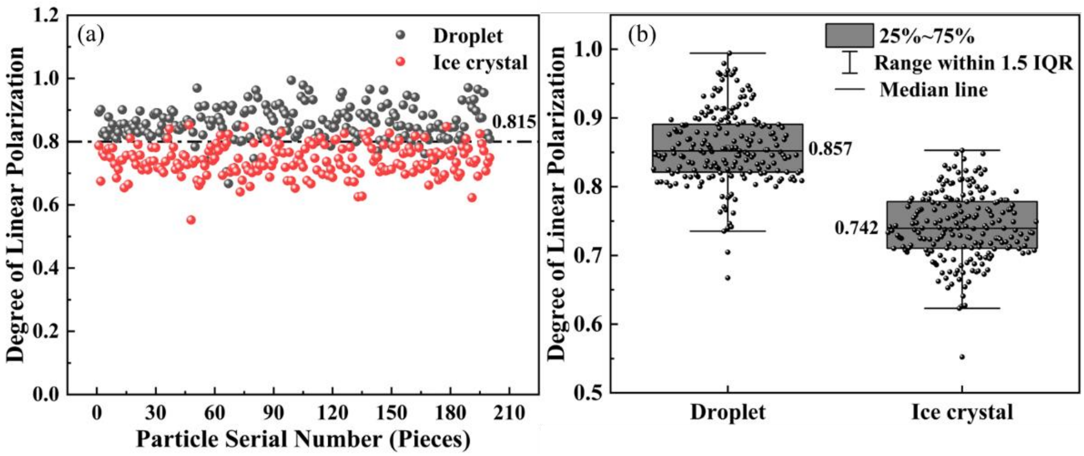

Figure 7: (a) Scatter plot of the degree of linear polarization (DoLP) for liquid droplets and ice crystals; (b) box plot of DoLP distributions for liquid droplets and ice crystals.

5 Discussion

These results indicate that both the circularity and the degree of linear polarization (DoLP) provide effective discrimination between liquid droplets and ice crystals. However, neither parameter alone is sufficient for complete phase separation. We therefore combined the morphological parameter (circularity) with the polarization parameter (DoLP) to improve classification accuracy. Integrating these complementary features enables more robust cloud particle phase identification.

https://doi.org/10.5194/egusphere-2026-3702
Preprint. Discussion started: 14 August 2026

We used a linear support vector machine (SVM) to classify liquid droplets and ice crystals on the basis of two features: the circularity and degree of linear polarization (DoLP). A linear SVM is a binary classifier grounded in statistical learning theory that seeks an optimal hyperplane in feature space by maximizing the margin between classes (Hastie et al., 2009). Given a training set $\{(\boldsymbol{x}_i, y_i)\}n_{i=1}$, where $\boldsymbol{x}_i \in \mathbb{R}^d$ denotes the feature vector, n is the number of training samples, d is the feature dimension, and $y_i \in \{-1, +1\}$ is the class label, with −1 for liquid droplets and +1 for ice crystals, the optimization problem can be written as (Guo and Wang, 2019)

$$\begin{gathered} \min_{\boldsymbol{w},b} \frac{1}{2}\|\boldsymbol{w}\|^2 + C\sum_{i=1}^{n} \xi_i \\ y_i(\boldsymbol{w}^T\boldsymbol{x}_i + b) \geq 1 - \xi_i, i = 1, \cdots, n \\ \xi_i \geq 0, i = 1, \cdots, n \end{gathered} \tag{21}$$

where **w** denotes the normal vector of the hyperplane, and b is the bias term. The slack variables ξ_i allow some samples to violate the hard-margin constraints, thereby improving robustness to noise and outliers. The regularization parameter C controls the trade-off between model complexity and training error, helping to prevent overfitting and improve generalization.

The dual form of the optimization problem in Eq. (21) can be derived using the method of Lagrange multipliers, leading to the following decision function:

$$f(x) = sign\left(\sum_{i\in S} a_i y_i \boldsymbol{x}_i^T \boldsymbol{x} + b\right) \tag{22}$$

where α_i are the Lagrange multipliers, and S denotes the set of support vectors, that is, the training samples satisfying $\alpha_i >$ 0. These support vectors lie on the margin boundaries and determine the position of the optimal decision hyperplane.

In the present study, the feature vector $\boldsymbol{x} = [x_1, x_2]^T$ consists of two parameters: circularity (x_1) and the degree of linear polarization (x_2). Accordingly, the decision hyperplane can be expressed as

$$w_1x_1 + w_2x_2 + b = 0 \tag{23}$$

where w_1 and w_2 are the SVM weights corresponding to the circularity and DoLP, respectively.

The classification rule is defined as follows:

$$\begin{cases} w_1x_1 + w_2x_2 + b > 0 \\ w_1x_1 + w_2x_2 + b \leq 0 \end{cases} \tag{24}$$

Samples with decision-function values greater than 0 are classified as ice crystals, whereas those with values less than or equal to 0 are classified as liquid droplets.

To evaluate the performance of the model, four metrics were employed: accuracy, precision, recall, and the confusion matrix.

https://doi.org/10.5194/egusphere-2026-3702
Preprint. Discussion started: 14 August 2026

Accuracy is defined as the proportion of correctly classified samples among all samples and reflects the overall predictive performance of the model. It is given by Eq. (25):

$$\mathrm{Accuracy} = \frac{\mathrm{TP} + \mathrm{TN}}{\mathrm{TP} + \mathrm{FP} + \mathrm{TN} + \mathrm{FN}} \tag{25}$$

365 where TP, TN, FP, and FN denote true positives, true negatives, false positives, and false negatives, respectively. Higher accuracy indicates better overall classification performance.

Precision is defined as the proportion of correctly predicted positive samples among all samples predicted as positive, reflecting the reliability of positive predictions. It is given by Eq. (26):

$$\mathrm{Precision} = \frac{\mathrm{TP}}{\mathrm{TP} + \mathrm{FP}} \tag{26}$$

370 Recall is defined as the proportion of correctly predicted positive samples among all actual positive samples, measuring the model's ability to identify positive instances. It is given by Eq. (27):

$$\mathrm{Recall} = \frac{\mathrm{TP}}{\mathrm{TP} + \mathrm{FN}} \tag{27}$$

The confusion matrix provides a matrix-based representation of the classification results, illustrating the correspondence between true and predicted classes and enabling intuitive analysis of different types of classification errors.

375 We classified 400 particles, including 200 liquid droplets and 200 ice crystals, using two features: the circularity and degree of linear polarization (DoLP). The dataset was randomly split into training (70%) and test (30%) sets. As shown in Fig. 8a, the linear support vector machine (SVM) achieved a test accuracy of 98.33%, demonstrating the effectiveness of the dual-parameter SVM method for cloud particle phase identification. To further evaluate the contribution of different features, we compared phase identification based on single parameters with that based on the combined two-parameter feature space (circularity and DoLP). The corresponding confusion matrices are shown in Fig. 8b–d.

https://doi.org/10.5194/egusphere-2026-3702
Preprint. Discussion started: 14 August 2026

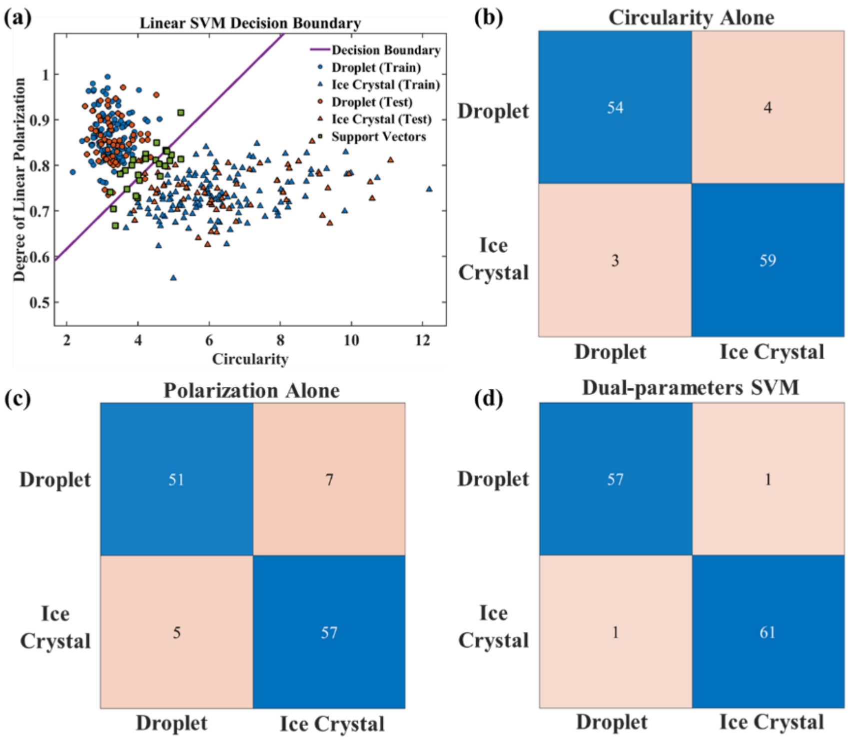

Figure 8: (a) Linear SVM decision boundary for classification of liquid droplets and ice crystals based on circularity and degree of linear polarization (DoLP); (b) confusion matrix based on circularity; (c) confusion matrix based on DoLP; (d) confusion matrix based on the dual-parameter SVM method.

Figure 8a shows the classification of liquid droplets and ice crystals using a linear support vector machine (SVM) based on two features: the circularity and degree of linear polarization (DoLP). Liquid droplets and ice crystals are denoted by circles and triangles, respectively, whereas training and test samples are distinguished by blue and orange colors. The solid line represents the decision boundary, and the support vectors near the margin are highlighted by square markers. Substituting the trained SVM coefficients into the general decision hyperplane given in Eq. (23), the specific decision function used in this study can be expressed as

$$0.0775x_1 - x_2 + 0.4552 = 0 \tag{28}$$

where x_1 and x_2 denote the circularity and DoLP, calculated from Eqs. (18) and (11), respectively, and w_1, w_2, and b are the trained SVM parameters with values $w_1 = 0.0775$, $w_2 = -1$, and $b = 0.4552$ obtained from the training set.

The classification rule of the linear SVM is as follows: samples with decision-function values greater than 0 are classified as ice crystals, whereas those with values less than or equal to 0 are classified as liquid droplets.

The confusion matrices show that using either the circularity or DoLP alone still leads to several cross-misclassifications, whereas the dual-parameter SVM method further reduces these errors. By contrast, the dual-parameter SVM method misclassifies only one sample in each class, substantially improving classification accuracy.

https://doi.org/10.5194/egusphere-2026-3702
Preprint. Discussion started: 14 August 2026

In addition, the accuracy, precision, and recall of the three identification approaches were calculated. Table 1 summarizes the comparative classification performance of these three methods.

Table 1: Comparison of classification performance for three identification methods

Method	Accuracy (%)	Precision (%)	Recall (%)
Circularity	94.17%	94.74%	93.10%
DoLP	90.00%	91.07%	87.93%
Dual-parameter	98.33%	98.28%	98.28%

The experimental results show that the dual-parameter SVM achieved the best classification performance. Relative to the single-parameter methods based on the circularity and degree of linear polarization (DoLP), the dual-parameter SVM method improved the accuracy by 4.16 and 8.33 percentage points, respectively, and precision by 3.54 and 7.21 percentage points, respectively. By integrating the circularity with DoLP, the dual-parameter SVM method achieves a better balance among accuracy, precision, and recall. While maintaining strong identification capability, it substantially reduces misclassification and markedly outperforms single-parameter methods overall.

To further examine the applicability of the polarization tomographic imaging method to dynamic microphysical observations of mixed-phase clouds, a continuous 10 s time window was selected from the late-stage cloud-chamber observation records after the introduction of the AgI catalyst. Liquid water content, the number concentrations of liquid droplets and ice crystals, and their particle-number fractions were then calculated. The liquid water content calculated using the circularity-threshold method and the dual-parameter method is shown in Fig. 9a. The LWC curves obtained by the two methods differ, mainly because the two phase-identification methods assign different classifications to borderline particles. Since LWC is proportional to the cube of particle diameter, the circularity-based method, which relies only on morphology, may misclassify relatively large quasi-spherical ice crystals as liquid droplets or misclassify liquid droplets affected by defocusing and noise as ice crystals, thereby leading to overestimation or underestimation of LWC. Although the curves obtained by the two methods are not identical, both show an overall decrease in LWC, indicating that supercooled liquid water in the cloud chamber was continuously consumed after AgI introduction. By contrast, the dual-parameter method combines both morphological and polarization information, thereby reducing phase misclassification of borderline particles. Therefore, in the subsequent analyses of particle number concentration and phase fraction, the dual-parameter classification results were used as the basis for phase classification to improve the reliability of microphysical statistics for mixed-phase particle ensembles.

The variations in the number concentrations of liquid droplets and ice crystals are shown in Fig. 9b. The droplet number concentration was initially relatively high and then decreased rapidly. This is because the selected time window was located in the late stage of mixed-phase cloud glaciation, when the cloud chamber had entered the liquid-phase depletion stage. Supercooled liquid droplets were continuously depleted through heterogeneous freezing, riming, and vapor competition between ice and liquid water, whereas the ice crystal number concentration fluctuated but remained at a certain level overall. Figure 9c further shows the variations in the particle-number fractions of liquid droplets and ice crystals. As time progressed,

https://doi.org/10.5194/egusphere-2026-3702
Preprint. Discussion started: 14 August 2026

the droplet fraction generally decreased, while the ice crystal fraction increased correspondingly, indicating that the phase composition of the particle ensemble in the cloud chamber gradually shifted from liquid-phase dominance toward an increased ice-phase fraction. In the subzero mixed-phase environment, the saturation vapor pressure over ice is lower than that over liquid water. As a result, the Wegener–Bergeron–Findeisen mechanism promotes vapor deposition onto ice crystal surfaces, while supercooled liquid droplets are also consumed through heterogeneous freezing and riming. Therefore, the observed decreases in LWC and droplet number concentration, together with the increase in the relative fraction of ice crystals, represent typical characteristics of mixed-phase cloud glaciation. These results indicate that the proposed polarization tomographic imaging method can not only achieve single-particle phase identification but also provide phase-resolved observations of number concentration and LWC, thereby providing an observational basis for characterizing the dynamic evolution of mixed-phase cloud particle ensembles.

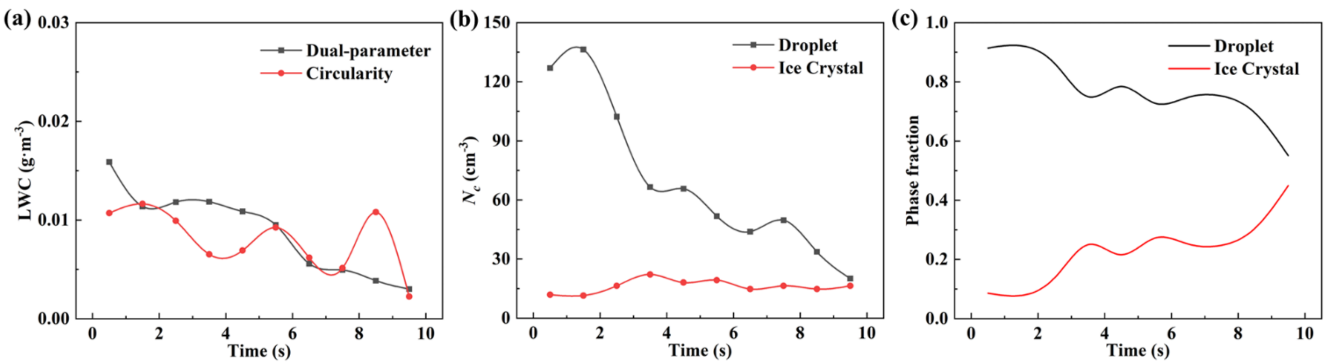

Figure 9: Microphysical evolution during the continuous 10 s time window in the late stage of mixed-phase cloud glaciation. (a) Liquid water content determined using the dual-parameter method and the circularity-threshold method; (b) number concentrations of liquid droplets and ice crystals determined using the dual-parameter method; (c) variations in the particle-number fractions of liquid droplets and ice crystals.

6 Conclusions

In this study, we developed a polarization tomographic imaging method that integrates digital holography with polarimetric imaging to enable phase identification of cloud particles smaller than 50 μm. The system allows the simultaneous retrieval of nine morphological parameters of individual particles within the field of view, including three-dimensional coordinates, particle size, area, perimeter, the major and minor axes of the minimum-area bounding rectangle, and circularity, together with four polarization parameters, namely the Stokes vector components and the degree of linear polarization (DoLP). Using the self-developed polarization tomographic imaging system, observation experiments of liquid droplets and ice crystals were conducted in an ice cloud chamber, and particle samples predominantly smaller than 50 μm were obtained for both phase types. The results show that droplet diameters were mainly distributed between 2.7 and 8.9 μm, with a mean circularity of approximately 3.32 and a mean DoLP of approximately 0.857. By contrast, ice crystals exhibited a broader size distribution, ranging from 8.9 to 53.3 μm, with a mean circularity of approximately 6.30 and a mean DoLP of approximately 0.742. The

https://doi.org/10.5194/egusphere-2026-3702
Preprint. Discussion started: 14 August 2026

two particle types showed distinct differences in both circularity and DoLP, but the distributions of each individual parameter still overlapped, making complete phase separation difficult. In particular, when ice crystal morphology approached a spherical shape, the discriminating capability of circularity decreased, whereas DoLP served as an important complementary indicator for phase identification. To improve phase-identification accuracy, circularity and DoLP were jointly used, and a linear support vector machine was applied to fit the two-parameter feature space and establish a phase-identification model. The classification accuracy reached 98.33%, representing a substantial improvement over single-parameter methods.

On this basis, a continuous 10 s observation window in the late stage of mixed-phase cloud glaciation during the ice cloud chamber experiment was selected to calculate liquid water content, the number concentrations of liquid droplets and ice crystals, and their particle-number fractions. The results show that LWC and droplet number concentration decreased overall with time, the droplet fraction gradually decreased, and the relative fraction of ice crystals increased, indicating that supercooled liquid water in the cloud chamber was continuously consumed and that the particle ensemble transitioned from liquid-phase dominance toward a mixed-phase state with an enhanced ice-phase contribution. Compared with the circularity-threshold method, the dual-parameter method can reduce the influence of phase misclassification of borderline particles on LWC statistics, thereby providing more reliable phase-resolved microphysical observations. From the perspective of cloud microphysics, this evolution can be attributed to ice – liquid interactions in a subzero mixed-phase environment. Because the saturation vapor pressure over ice is lower than that over liquid water, vapor is more likely to deposit onto ice crystal surfaces, while supercooled liquid droplets are further consumed through heterogeneous freezing, riming, and vapor competition between ice and liquid water. Therefore, the dynamic observations are consistent with the Wegener-Bergeron-Findeisen mechanism and the glaciation process of mixed-phase clouds. These results indicate that the proposed polarization tomographic imaging method can not only achieve high-accuracy single-particle phase identification for small-scale cloud particles but also provide microphysical observations such as number concentration, particle-number fraction, and liquid water content, which can be used to characterize the dynamic evolution of mixed-phase cloud particle ensembles. This method has potential application value in studies of mixed-phase cloud microphysical processes, cloud microphysical parameter observations, and the assessment of operational conditions for weather modification.

Appendix A: Ice cloud chamber experimental environment and operating procedure

Observation experiments of droplets and ice crystals were conducted in an ice cloud chamber using the polarization tomography imaging system. The experimental environment and working procedure of the ice cloud chamber are shown in Fig. A1. Figure A1a shows the ice cloud chamber used in this study. The chamber is equipped with an observation window, which enables real-time observation of the generation and evolution of particles inside the chamber. During the experiment, the ice cloud chamber was maintained at constant pressure and under supersaturated conditions. Figure A1b illustrates the working procedure of the ice cloud chamber. First, a low-temperature environment was established using a low-temperature compressor, and droplets were generated using an ultrasonic atomizer. The droplets then diffused through free thermal

https://doi.org/10.5194/egusphere-2026-3702
Preprint. Discussion started: 14 August 2026

convection to form supercooled water droplets. In the absence of catalyst injection, the chamber mainly contained liquid supercooled water droplets. Subsequently, high-concentration AgI smoke, generated by burning silver iodide (AgI) smoke agent in a sealed container, was introduced into the chamber through a gas tube to catalyze ice crystal formation. The supercooled water droplets underwent heterogeneous freezing with AgI aerosol particles acting as ice nuclei and further grew under the supercooled water environment in the chamber through vapor deposition, collision–coalescence, and riming processes. The generated ice crystals then settled under gravity into the observation region of the polarization tomography imaging system, enabling simultaneous observation of mixed-phase particles consisting of droplets and ice crystals. When the ice crystal coverage density on the observation window became too high to clearly distinguish the morphology and structure of individual ice crystals, the window was manually cleaned with anhydrous ethanol, and a new cycle of ice crystal preparation and observation was then performed.

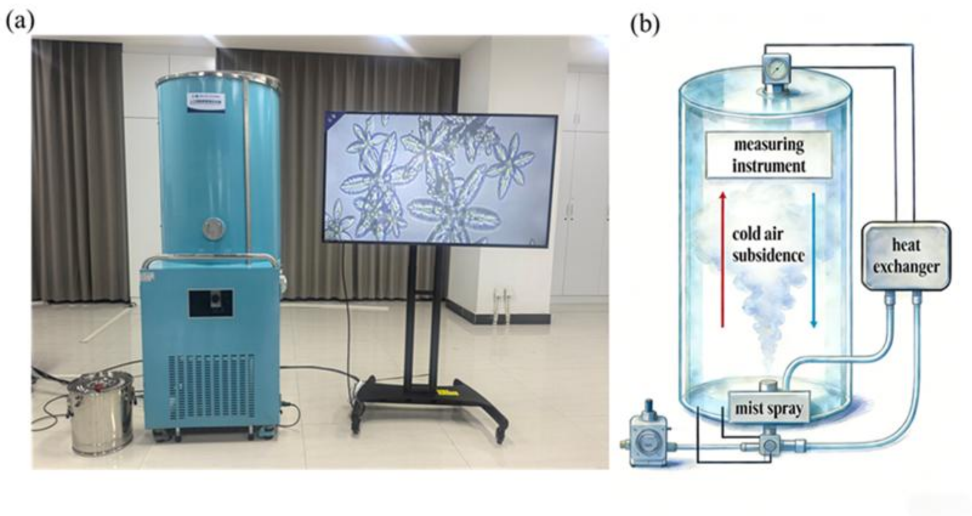

Figure A1. (a) Experimental environment of the ice cloud chamber; (b) working procedure of the ice cloud chamber.

Appendix B: Morphological parameters of representative particles

To demonstrate the capability of the polarization tomographic imaging system to extract morphological parameters of individual particles, Fig. 2 in the main text summarizes the morphological analysis process of four representative particles, including one liquid droplet (a) and three ice crystals (b–d). After binarization, edge smoothing, hole filling, contour extraction, and minimum-area bounding rectangle fitting were performed on the in-focus particle images, morphological parameters including the three-dimensional coordinates, projected-area equivalent diameter, major and minor axes of the minimum-area bounding rectangle, perimeter, area, and circularity were obtained. The detailed parameters of the four particles are summarized in Table B1.

Table B1: Morphological parameters of the four representative particles shown in Fig. 2.

Particle	*x* (mm)	*y* (mm)	*z* (mm)	Area-equivalent diameter (μm)	Minor Axis (μm)	Major Axis (μm)	Perimeter (μm)	Projected area (μm^2)	Circularity *F*
a	1.578	0.29	1.2	4.335	3.3944	4.0115	11.767	15.711	3.016
b	0.743	0.169	0.72	20.775	13.944	36.423	121.12	448.49	9.84
c	0.172	0.428	0.12	19.62	18.63	20.01	63.546	318.03	4.01
d	0.415	0.799	0.16	24.023	23.58	24.995	80.991	482.29	4.2

Code and data availability

The source code used for particle image processing, morphological and polarization-parameter extraction, and dual-parameter SVM phase classification is archived on Zenodo and available at https://doi.org/10.5281/zenodo.20424416 under the MIT License. The experimental datasets supporting this study, including calibration measurements, particle morphological and polarization parameters, particle labels, train/test split information, classification results, liquid water content, droplet and ice crystal number concentrations, particle-number fractions, and the data underlying the figures and tables, are archived on Zenodo and available at https://doi.org/10.5281/zenodo.20809317 under the Creative Commons Attribution 4.0 International license.

Author contributions

YC developed the method, performed the experiments and data analysis, prepared the figures and tables, and wrote the manuscript. XX conceived and supervised the study, guided the optical-system design and data interpretation, and revised the manuscript. RX contributed to system construction, cloud-chamber observations, image processing, and parameter analysis. FY, XS, JiaW, and JunW assisted with the experiments, data processing, and result validation. GL and ZY designed the ice cloud chamber experiments and provided the experimental site, chamber conditions, and technical support. All authors reviewed and approved the final manuscript.

Competing interests

The authors declare that they have no competing interests.

Acknowledgements

The authors acknowledge financial support from the National Natural Science Foundation of China and the Shaanxi Provincial Key Research and Development Program. The authors also thank the Weather Modification Center of Shaanxi Province for providing the ice cloud chamber experimental site, experimental conditions, and technical support during the experiments.

https://doi.org/10.5194/egusphere-2026-3702
Preprint. Discussion started: 14 August 2026

Financial support

This research has been supported by the National Natural Science Foundation of China (grant no. 42575150) and the Shaanxi Provincial Key Research and Development Program (grant no. 2024NC-YBXM-062).

References

Aviles, K. M. and Lear, B. J.: Practical guide to automated TEM image analysis for increased accuracy and precision in the measurement of particle size and morphology, ACS Nanosci. Au, 5, 117–127, https://doi.org/10.1021/acsnanoscienceau.4c00076, 2025.

Bass, M., Van Stryland, E. W., Williams, D. R., and Wolfe, W. L.: Handbook of optics, McGraw-Hill, New York, NY, 1995.

Behal, J., Valentino, M., Miccio, L., Bianco, V., Itri, S., Mossotti, R., Fontana, G. D., Stella, E., and Ferraro, P.: Toward an all-optical fingerprint of synthetic and natural microplastic fibers by polarization-sensitive holographic microscopy, ACS Photonics, 9, 694–705, https://doi.org/10.1021/acsphotonics.1c01781, 2022.

Born, M. and Wolf, E.: Principles of optics: Electromagnetic theory of propagation, interference and diffraction of light, Elsevier, 2013.

Cazac, V., Achimova, E., Abashkin, V., Loshmanskii, C., Botnari, V., and Toy, M. F.: Birefringence mapping of diffractive optical elements on gold-doped azopolymer nanocomposites by polarization digital holographic microscopy, in: IFMBE Proceedings, 7th International Conference on Nanotechnologies and Biomedical Engineering, Cham, 151–161, https://doi.org/10.1007/978-3-032-06494-3_17, 2025.

Chen, Y., Xu, X., Xiao, R., Yao, F., Shi, X., and Wang, J.: Data for publication "Single-Particle Polarization Tomography Enables Highly Accurate Phase Identification of Cloud Particles", Zenodo [data set], https://doi.org/10.5281/zenodo.20809317, 2026a.

Chen, Y., Xu, X., Xiao, R., Yao, F., Shi, X., and Wang, J.: Code for publication "Single-Particle Polarization Tomography Enables Highly Accurate Phase Identification of Cloud Particles", Zenodo [code], https://doi.org/10.5281/zenodo.20424416, 2026b.

D'Alessandro, J. J., McFarquhar, G. M., Stith, J. L., Diao, M., DeMott, P. J., McCluskey, C. S., Hill, T. C. J., Roberts, G. C., and Sanchez, K. J.: An evaluation of phase, aerosol‐cloud interactions and microphysical properties of single‐ and multi‐layer clouds over the Southern Ocean using in situ observations from SOCRATES, J. Geophys. Res.-Atmos., 128, e2023JD038610, https://doi.org/10.1029/2023JD038610, 2023.

Donovan, D. P., Baltink, H. K., Henzing, J. S., Roode, S. R. d., and Siebesma, A. P.: A depolarisation lidar-based method for the determination of liquid-cloud microphysical properties, Atmos. Meas. Tech., 8, 237–266, https://doi.org/10.5194/amt-8-237-2015, 2015.

Dubovik, O., Li, Z., Mishchenko, M. I., Tanre, D., Karol, Y., Bojkov, B., Cairns, B., Diner, D. J., Espinosa, W. R., Goloub, P., Gu, X., Hasekamp, O., Hong, J., Hou, W., Knobelspiesse, K. D., Landgraf, J., Li, Litvinov, P., Liu, Y., Lopatin, A., Marbach, T., Maring, H., Martins, V., Meijer, Y., Milinevsky, G., Mukai, S., Parol, F., Qiao, Y., Remer, L., Rietjens, J., Sano, I., Stammes, P., Stamnes, S., Sun, X., Tabary, P., Travis, L. D., Waquet, F., Xu, F., Yan, C., and Yin, D.: Polarimetric remote sensing of atmospheric aerosols: Instruments, methodologies, results, and perspectives, J. Quant. Spectrosc. Radiat. Transf., 224, 474–511, https://doi.org/10.1016/j.jqsrt.2018.11.024, 2019.

Ewald, F., Gross, S., Wirth, M., Delanoe, J., Fox, S., and Mayer, B.: Why we need radar, lidar, and solar radiance observations to constrain ice cloud microphysics, Atmos. Meas. Tech., 14, 5029–5047, https://doi.org/10.5194/amt-14-5029-2021, 2021.

Fuller, G. G.: Optical rheometry of complex fluids, Oxford University Press, New York, NY, 1995.

Gao, P., Wang, J., Tang, J., Gao, Y., Liu, J., Yan, Q., and Hua, D.: Investigation of cloud droplets velocity extraction based on depth expansion and self-fusion of reconstructed hologram, Opt. Express, 30, 18713–18729, https://doi.org/10.1364/oe.458947, 2022.

Gaudek, T., Jimenez, C., Ohneiser, K., Fuchs, C., Henneberger, J., Bühl, J., Klamt, A., Ansmann, A., Engelmann, R., and Seifert, P.: Contribution of the 2DVD to the investigation of cloud microphysics during the MOSAiC and CloudLab/PolarCAP campaigns, Atmos. Meas. Tech., 19, 2245–2263, https://doi.org/10.5194/amt-19-2245-2026, 2026.

Georgakaki, P., Billault-Roux, A.-C., Foskinis, R., Gao, K., Sotiropoulou, G., Gini, M., Takahama, S., Eleftheriadis, K., Papayannis, A., Berne, A., and Nenes, A.: Unraveling ice multiplication in winter orographic clouds via in-situ observations, remote sensing and modeling, npj Clim. Atmos. Sci., 7, 145, https://doi.org/10.1038/s41612-024-00671-9, 2024.

Guo, H. and Wang, W.: Granular support vector machine: A review, Artif. Intell. Rev., 51, 19–32, https://doi.org/10.1007/s10462-017-9555-5, 2019.

Hastie, T., Tibshirani, R., and Friedman, J.: Support vector machines and flexible discriminants, in: The elements of statistical learning: Data mining, inference, and prediction, Springer, New York, NY, 417–458, https://doi.org/10.1007/978-0-387-84858-7_12, 2009.

Hong, Y., Kang, G., Zang, J., Fan, F., Liu, Y., Tan, X., Shimura, T., and Kuroda, K.: Investigation of faithful reconstruction in nonparaxial approximation polarization holography, Appl. Opt., 56, 10024–10029, https://doi.org/10.1364/ao.56.010024, 2017.

Huang, M. and Lei, H.: An improved Holroyd cloud particle habit identification method and its application, Acta Meteorol. Sin., 78, 289–300, https://doi.org/10.11676/qxxb2020.018, 2020.

Huang, Z., Li, M., Bi, J., Shen, X., Zhang, S., and Liu, Q.: Small lidar ratio of dust aerosol observed by Raman-polarization lidar near desert sources, Opt. Express, 31, 16909–16922, https://doi.org/10.1364/oe.484501, 2023.

Jordan, T. M., Schroeder, D. M., Castelletti, D., Li, J., and Dall, J.: A polarimetric coherence method to determine ice crystal orientation fabric from radar sounding: Application to the NEEM ice core region, IEEE Trans. Geosci. Remote Sens., 57, 8641–8657, https://doi.org/10.1109/tgrs.2019.2921980, 2019.

Knopf, D. A. and Alpert, P. A.: Atmospheric ice nucleation, Nat. Rev. Phys., 5, 203–217, https://doi.org/10.1038/s42254-023-00570-7, 2023.

Lane, C., Rode, D., and Rösgen, T.: Two-dimensional birefringence measurement technique using a polarization camera, Appl. Opt., 60, 8435–8444, https://doi.org/10.1364/ao.433066, 2021.

Liu, B., Fang, X., Tian, A., Wang, S., Zhang, R., Wang, H., and Zhu, X.: Parallel phase-shifting digital holographic phase imaging of micro-optical elements with a polarization camera, Photonics, 10, 1291, https://doi.org/10.3390/photonics10121291, 2023.

Liu, Z., Takahashi, T., Lindsay, D., Thevar, T., Sangekar, M., Watanabe, H. K., Burns, N., Watson, J., and Thornton, B.: Digital in-line holography for large-volume analysis of vertical motion of microscale marine plankton and other particles, IEEE J. Oceanic Eng., 46, 1248–1260, https://doi.org/10.1109/joe.2021.3066788, 2021.

Luke, E. P., Yang, F., Kollias, P., Vogelmann, A. M., and Maahn, M.: New insights into ice multiplication using remote-sensing observations of slightly supercooled mixed-phase clouds in the Arctic, P. Natl. Acad. Sci. USA, 118, e2021387118, https://doi.org/10.1073/pnas.2021387118, 2021.

Ma, X., Zhao, H., Zhang, Y., Mao, J., Zhou, C., Gong, X., Rao, Z., Bu, L., and Hua, D.: Investigation of full polarization characteristics of aerosols and cloud particles with Stokes lidar, Opt. Lasers Eng., 192, 109034, https://doi.org/10.1016/j.optlaseng.2025.109034, 2025.

Matus, A. V. and L'Ecuyer, T. S.: The role of cloud phase in Earth's radiation budget, J. Geophys. Res.-Atmos., 122, 2559–2578, https://doi.org/10.1002/2016JD025951, 2017.

Morrison, H., Lier-Walqui, M. v., Fridlind, A. M., Grabowski, W. W., Harrington, J. Y., Hoose, C., Korolev, A., Kumjian, M. R., Milbrandt, J. A., Pawlowska, H., Posselt, D. J., Prat, O. P., Reimel, K. J., Shima, S.-I., Diedenhoven, B. v., and Xue, L.: Confronting the challenge of modeling cloud and precipitation microphysics, J. Adv. Model. Earth Syst., 12, e2019MS001689, https://doi.org/10.1029/2019MS001689, 2020.

Pan, G., Jun, W., Cheng-Cheng, Z., Jia-Bin, T., Jing-Jing, L., Qing, Y., and Deng-Xin, H.: Simultaneous measurement of cloud microphysical parameters based on digital holographic interferometry, Acta Phys. Sin., 70, 099201, https://doi.org/10.7498/aps.70.20201779, 2021.

Pettersen, C., Bliven, L. F., Kulie, M. S., Wood, N. B., Shates, J. A., Anderson, J., Mateling, M. E., Petersen, W. A., Lerber, A. v., and Wolff, D. B.: The precipitation imaging package: Phase partitioning capabilities, Remote Sens., 13, 2183, https://doi.org/10.3390/rs13112183, 2021.

Phillips, V. T. J.: A theory for the balance between warm rain and ice crystal processes of precipitation in mixed-phase clouds, J. Atmos. Sci., 81, 317–339, https://doi.org/10.1175/jas-d-23-0054.1, 2024.

https://doi.org/10.5194/egusphere-2026-3702
Preprint. Discussion started: 14 August 2026

Qi, S., Huang, Z., Ma, X., Huang, J., Zhou, T., Zhang, S., Dong, Q., Bi, J., and Shi, J.: Classification of atmospheric aerosols and clouds by use of dual-polarization lidar measurements, Opt. Express, 29, 23461–23476, https://doi.org/10.1364/oe.430456, 2021.

Schlimme, I., Macke, A., and Reichardt, J.: The impact of ice crystal shapes, size distributions, and spatial structures of cirrus clouds on solar radiative fluxes, J. Atmos. Sci., 62, 2274–2283, https://doi.org/10.1175/jas3459.1, 2005.

Shcherbakov, V., Szczap, F., Mioche, G., and Cornet, C.: Multiple-scattering effects on single-wavelength lidar sounding of multi-layered clouds, Atmos. Meas. Tech., 17, 3011–3028, https://doi.org/10.5194/amt-17-3011-2024, 2024.

Shishko, V. A., Timofeev, D. N., Konoshonkin, A. V., Kustova, N. V., Kan, N., Tkachev, I. V., Masuda, K., Ishimoto, H., Okamoto, H., and Borovoi, A. G.: Backscattering characteristics of optical and electromagnetic waves in joint sensing of cirrus clouds by a polarizing lidar (0.355 μm) and a 94-GHz radar, Atmos. Ocean. Opt., 35, S182–S182, https://doi.org/10.1134/s1024856022060239, 2023.

Singh, D. K. and Panigrahi, P. K.: Improved digital holographic reconstruction algorithm for depth error reduction and elimination of out-of-focus particles, Opt. Express, 18, 2426–2448, https://doi.org/10.1364/oe.18.002426, 2010.

Wang, J., Chen, J., Yu, F., Chen, R., Wang, J., Zhao, Z., Li, X., Xing, H., Li, G., Chen, X., and Lu, W.: Unlocking ultra-high holographic information capacity through nonorthogonal polarization multiplexing, Nat. Commun., 15, 6284, https://doi.org/10.1038/s41467-024-50586-5, 2024.

Wieder, J., Ihn, N., Mignani, C., Haarig, M., Buehl, J., Seifert, P., Engelmann, R., Ramelli, F., Kanji, Z. A., Lohmann, U., and Henneberger, J.: Retrieving ice nucleating particle concentration and ice multiplication factors using active remote sensing validated by in situ observations, Atmos. Chem. Phys., 22, 9767–9797, https://doi.org/10.5194/acp-22-9767-2022, 2022.

Xiao, D., Wang, N., Chen, S., Wu, L., Mueller, D., Veselovskii, I., Li, C., Landulfo, E., Sivakumar, V., Li, J., Che, H., Fang, J., Zhang, K., Wang, B., Chen, F., Hu, X., Li, X., Li, W., Tong, Y., Ke, J., Wu, L., Liu, C., and Liu, D.: Simultaneous profiling of dust aerosol mass concentration and optical properties with polarized high-spectral-resolution lidar, Sci. Total Environ., 872, 162091, https://doi.org/10.1016/j.scitotenv.2023.162091, 2023.

Xu, Z., Hua, H., Yu, J., Niu, Z., and Kong, M.: Research on synchronous inversion algorithm based on tri-wavelength DIAL, Optics, 6, 48, https://doi.org/10.3390/opt6040048, 2025.

Yan, L., Qi, P., Zhang, L., Goudail, F., Liu, T., Zhai, J., and Hu, H.: Polarimetric imaging via deep learning: A review, Remote Sens., 15, 1540, https://doi.org/10.3390/rs15061540, 2023.

Yan, L., Wu, K., Lin, J., Xu, X., Zhang, J., Zhao, X., Tayor, J., and Chen, D.: Identification and picking point positioning of tender tea shoots based on MR3P-TS model, Front. Plant Sci., 13, 962391, https://doi.org/10.3389/fpls.2022.962391, 2022.

Zhang, Y., Zhao, J., Di, J., Jiang, H., Wang, Q., Wang, J., Guo, Y., and Yin, D.: Real-time monitoring of the solution concentration variation during the crystallization process of protein-lysozyme by using digital holographic interferometry, Opt. Express, 20, 18415–18421, https://doi.org/10.1364/oe.20.018415, 2012.

Zhou, G., Wang, J., Yin, Y., Hu, X., Letu, H., Sohn, B.-J., Yung, Y. L., and Liu, C.: Detecting supercooled water clouds using passive radiometer measurements, Geophys. Res. Lett., 49, e2021GL096111, https://doi.org/10.1029/2021gl096111, 2022a.

Zhou, H., Li, J., Liao, R., Chen, Y., Liu, T., Wang, Y., Zhang, X., and Ma, H.: Profile probing of suspended particles in water by Stokes vector polarimetry, Opt. Express, 30, 14924–14937, https://doi.org/10.1364/oe.455288, 2022b.